Relationships between Marine Stratus Cloud Optical Depth and Temperature: Inferences from AVHRR Observations

FU-LUNG CHANG

National Institute of Aerospace, Hampton, Virginia

JAMES A. COAKLEY JR.

College of Oceanic and Atmospheric Sciences, Oregon State University, Corvallis, Oregon

(Manuscript received 9 March 2006, in final form 7 August 2006)

ABSTRACT

Studies using International Satellite Cloud Climatology Project (ISCCP) data have reported decreases in cloud optical depth with increasing temperature, thereby suggesting a positive feedback in cloud optical depth as climate warms. The negative cloud optical depth and temperature relationships are questioned because ISCCP employs threshold assumptions to identify cloudy pixels that have included partly cloudy pixels. This study applies the spatial coherence technique to one month of Advanced Very High Resolution Radiometer (AVHRR) data over the Pacific Ocean to differentiate overcast pixels from the partly cloudy pixels and to reexamine the cloud optical depth–temperature relationships. For low-level marine stratus clouds studied here, retrievals from partly cloudy pixels showed 30%–50% smaller optical depths, 1°–4°C higher cloud temperatures, and slightly larger droplet effective radii, when they were compared to retrievals from the overcast pixels. Despite these biases, retrievals for the overcast and partly cloudy pixels show similar negative cloud optical depth–temperature relationships and their magnitudes agree with the ISCCP results for the midlatitude and subtropical regions. There were slightly negative droplet effective radius–temperature relationships, and considerable positive cloud liquid water content–temperature relationships indicated by aircraft measurements. However, cloud thickness decreases appear to be the main reason why cloud optical depth decreases with increasing temperature. Overall, cloud thickness thinning may explain why similar negative cloud optical depth–temperature relationships are found in both overcast and partly cloudy pixels. In addition, comparing the cloud-top temperature to the air temperature at 740 hPa indicates that cloud-top height generally rises with warming. This suggests that the cloud thinning is mainly due to the ascending of cloud base. The results presented in this study are confined to the midlatitude and subtropical Pacific and may not be applicable to the Tropics or other regions.

1. Introduction

Cloud feedback is one of the largest sources of uncertainties in climate sensitivity studies from general circulation models (GCMs; Cubasch et al. 2001; Stephens 2005). The interaction of radiation with cloud optical properties, in particular, cloud optical depth, can significantly alter the amount of radiative energy flow that enters and leaves the earth's surface and atmosphere (e.g., Wielicki et al. 1995, 1996; Houghton et al. 1996). The strong impact of clouds on the earth–atmosphere radiation budget plays a key factor in determining the climate system, but potential changes in cloud optical properties associated with climate change may induce feedback processes that in turn influence the climate variability. It has been demonstrated that altering the way in which cloud–climate feedback mechanisms are represented in GCMs can lead to differences by a factor of 3 in global climate sensitivities among GCMs (Cess et al. 1990). Today, simulating realistic cloud feedbacks in climate modeling remains elusive. Whether cloud will feed back in a positive or negative way on the climate variability is uncertain because large discrepancies in the magnitude and sign of cloud–climate feedbacks still exist among current GCMs (Cess et al. 1990, 1996; Senior and Mitchell 1993; Yao and Del Genio 1999).

Corresponding author address: Dr. Fu-Lung Chang, National Institute of Aerospace (NIA), 100 Exploration Way, Room 214, Hampton, VA 23666-6147.
E-mail: f.chang@larc.nasa.gov

DOI: 10.1175/JCLI4115.1

Clouds may influence to climate change in different ways. This paper is concerned with the temperature-dependent cloud optical depth feedback. Early arguments on the temperature-dependent cloud optical depth feedback (e.g., Somerville and Remer 1984; Betts and Harshvandhan 1987) are related to the variations of cloud liquid water content (LWC) with temperature (T). For instance, Somerville and Remer (1984), based on empirical relationships between cloud LWC and T derived using aircraft measurements of more than 20 000 flights into clouds over the former Soviet Union (Feigelson 1978), suggested a negative cloud optical depth feedback—the cloud optical depth increases with increasing temperature, which would in turn diminish the effects of a climate warming. They suggested that cloud LWC increased as the atmosphere warmed at the rate of $d\ \ln(\mathrm{LWC})/dT = +0.04$ to $+0.05$ for T between $-25°$ and $+5°\mathrm{C}$. These results are supported by the adiabatic calculations from Betts and Harshvardhan (1987), who calculated this rate of increase based on adiabatic ascent of moist parcels. The positive values of $d\ \ln(\mathrm{LWC})/dT$ suggest that, if all other cloud properties such as cloud cover fraction and cloud altitude remain the same, the cloud optical depth will increase and thus reflect more sunlight back to space as the climate warms, which implies a negative feedback to a climate warming.

Satellite observations, like the International Satellite Cloud Climatology Project (ISCCP; Rossow et al. 1991), provide global measurements of cloud optical depth and temperature. The ISCCP data have been used to study the cloud optical depth and temperature relationships (Tselioudis et al. 1992; Tselioudis and Rossow 1994). In particular, for low-level clouds Tselioudis et al. (1992) found a negative relationship between the ISCCP low-cloud optical depth, τ, and temperature, T, and they suggested that the optical depth of warm clouds decreased with increased temperature at the rate of $d\ \ln\tau/dT \approx -0.04$. The negative values of $d\ \ln\tau/dT$ suggest that clouds would become optically thinner as the climate becomes warmer, implying a positive cloud optical depth feedback to a climate warming.

The negative values of $d\ \ln\tau/dT$ derived from the ISCCP data have raised the question of whether cloud optical depth indeed decreased with increased temperature or not. The reason is that ISCCP cloud properties were derived based on the threshold assumption that satellite pixels identified as being cloudy were completely overcast, even if they were only partly cloud covered. The threshold assumption can lead to biased cloud properties in partly cloudy pixels (Chang and Coakley 1993; Harshvardhan et al. 1994), typically cloud optical depths that are underestimated and cloud temperatures that are overestimated (Coakley et al. 2005). This may be one reason why there are negative cloud optical depth–temperature relationships in the ISCCP data. If the pixel-scale cloudiness went from largely overcast to partly cloudy, then ISCCP data would suggest that cloud optical depth decreased while cloud temperature increased. Clearly, variations in pixel-scale cloud cover fraction can explain the negative relationships between cloud optical depth and temperature inferred by the ISCCP products.

This study used the Advanced Very High Resolution Radiometer (AVHRR) 4-km global area coverage (GAC) satellite imagery data to reexamine the empirical relationships between cloud optical depth and temperature for low-level marine stratus clouds. One issue addressed here is whether the cloud optical depths of *overcast* pixels indeed decreased with increased temperature. Another is to evaluate the effects of partly cloudy pixels. This study applies the spatial coherence method (Coakley and Bretherton 1982; Coakley and Baldwin 1984) to differentiate overcast pixels from partly cloudy pixels. AVHRR data between 55°S and 55°N for the Pacific Ocean were analyzed for March 1989. The reexamination by separating the overcast pixels from partly cloudy pixels is important to understand the limitation of the threshold assumption and thus the validity of the cloud optical depth and temperature relationships derived using the ISCCP data.

In the second part of the study, we explore the different relationships between cloud LWC and temperature reported in the literature. This includes comparisons between the thermodynamic calculations from the temperature-dependent adiabatic LWC of a rising air parcel (Betts and Harshvandhan 1987) and the aircraft-measured variations of cloud LWC with temperature reported in the literature (Feigelson 1978; Somerville and Remer 1984; Mazin 1995; Gultepe and Isaac 1997). The positive values of $d\ \ln(\mathrm{LWC})/dT$ derived by Betts and Harshvandhan (1987) have been widely used by many GCMs with a diagnostic cloud parameterization scheme, and these GCMs generally resulted in a negative cloud optical feedback effect (Cess et al. 1990). Despite many cloud field experiments around the globe, there are relatively few in situ observational data that are sufficient to verify the adiabatic values of $d\ \ln(\mathrm{LWC})/dT$ derived by Betts and Harshvandhan. Large databases with extensive aircraft measurements adequate to characterize cloud LWC and temperature relationships were mainly obtained for continental midlatitude regions (Feigelson 1978; Mazin 1995; Gultepe and Isaac 1997). These documented aircraft measurements of cloud LWC, while most representative of the northern midlatitude low clouds, are explored in this study to evaluate the cloud LWC and temperature relationships and determine what factors dominated the behavior of satellite-observed cloud optical depth and temperature relationships.

Furthermore, the sensitivities of cloud optical depth, τ, droplet effective radius, r_e, and cloud layer temperature, T_c, derived from the overcast pixels are evaluated against the 740-hPa atmospheric temperature, T. An increase or decrease in cloud layer temperature itself may be decoupled from the atmospheric warming, which is determined by the rate of change in dT_c/dT. A positive value of dT_c/dT indicates that cloud layer altitude decreases with atmospheric warming whereas a negative value indicates that cloud layer altitude increases with atmospheric warming. The cloud geometrical thickness, D, is then estimated by a simple relationship between cloud optical depth, LWC, and droplet effective radius. Taken together, we examine the sensitivity parameters of τ, r_e, LWC, and D to T_c and T defined as the logarithmic derivative with respect to temperature, for example, $d\ln\tau/dT_c$, $d\ln r_e/dT_c$, $d\ln(\mathrm{LWC})/dT_c$, and $d\ln D/dT_c$. These sensitivity parameters are examined for the Pacific Ocean for northern midlatitudes between 25° and 55°N and for 2.5° latitudinal variations from 55°S to 55°N. Values of dT_c/dT are used to infer the possible trend of cloud-top height variations with atmospheric warming. Variations of cloud-base height can then be inferred from variations in both dT_c/dT and $d\ln D/dT$. In the next section, we describe the satellite data and cloud property retrievals for the overcast and partly cloudy pixels. Section 3 presents the results and discussions and section 4 gives the conclusions.

2. The satellite data and retrieval algorithm

a. The spatial coherence method and threshold cloud detection

AVHRR GAC data were analyzed for daytime passes between 55°S and 55°N over the Pacific Ocean for March 1989. The AVHRR is a scanning radiometer, onboard the *NOAA-11* polar-orbiting satellite, which measured multispectral radiances in five channels at nominally 0.63-, 0.89-, 3.7-, 11-, and 12-μm wavelengths (Kidwell 1991). The GAC format is a spatially convolved version of AVHRR imagery with a nominal resolution of ~4 km at nadir. The 0.63-, 3.7-, and 11-μm observations were used in this study for cloud property retrievals. The swath of AVHRR measurements covered approximately 2400 km cross track. Each measuring segment along track lasts for approximately 30 min from 55°S to 55°N. On each day, there were usually five daytime passes over the Pacific Ocean. A total of about 150 AVHRR daytime passes were analyzed for March 1989.

Satellite cloud property retrievals are divided into two steps: first is the scene identification, and then the retrieval of cloud properties follows. Radiance threshold methods, like those used by ISCCP (Rossow et al. 1991), are commonly employed to identify cloudy pixels that are used for cloud property retrievals. In the threshold methods, predefined values for solar reflectance (visible channel) and brightness temperature (infrared channel) are used to differentiate between cloudy and cloud-free pixels. Each pixel, however, is treated as being either completely overcast or completely cloud free. Undoubtedly, many of the threshold cloudy pixels can only be partly cloudy. The cloud-free portion within a partly cloudy pixel thus leads to biased cloud properties, for example, cloud optical depth being underestimated and cloud layer temperature being overestimated due to contamination from the radiances of the cloud-free portion.

To eliminate biases from partly cloudy pixels, the spatial coherence method (Coakley and Bretherton 1982) was used to discriminate between cloudy pixels that were overcast by clouds that constituted a single cloud layer and pixels that were only partially covered, or overcast by clouds that were distributed in altitude. The spatial coherence method takes advantage of the stratification of the atmosphere, which results in many cloud systems forming well-defined layers. Maritime stratus and stratocumulus are typical of such cloud systems that have relatively uniform layer temperatures over regions spanning several hundred kilometers. Such clouds often congregate so that arrays of the 11-μm imager pixels exhibit spatially uniform infrared brightness temperatures.

Figure 1a illustrates an example of the spatial coherence method applied to AVHRR 11-μm radiances for a 250-km scale region near the coast of Chile. The figure shows a spatial coherence arch that is typical of marine stratus and stratocumulus systems. The method examines the local spatial uniformity of the 11-μm emission for 2 × 2 arrays of adjacent pixels by calculating a local mean and a local standard deviation of the 11-μm radiances for each of the 2 × 2 arrays. Each symbol in the figure thus represents a local mean and a local standard deviation of an 8-km portion of the region. Figure 1a shows that the overcast pixels (solid circles) with near-zero standard deviations and similar 11-μm radiances near 88 mW m^{-2} sr^{-1} cm are clustered to form a foot of the arch. The other foot of the arch near 102 mW m^{-2} sr^{-1} cm is associated with the cloud-free pixels representing the brightness temperatures of the ocean back-

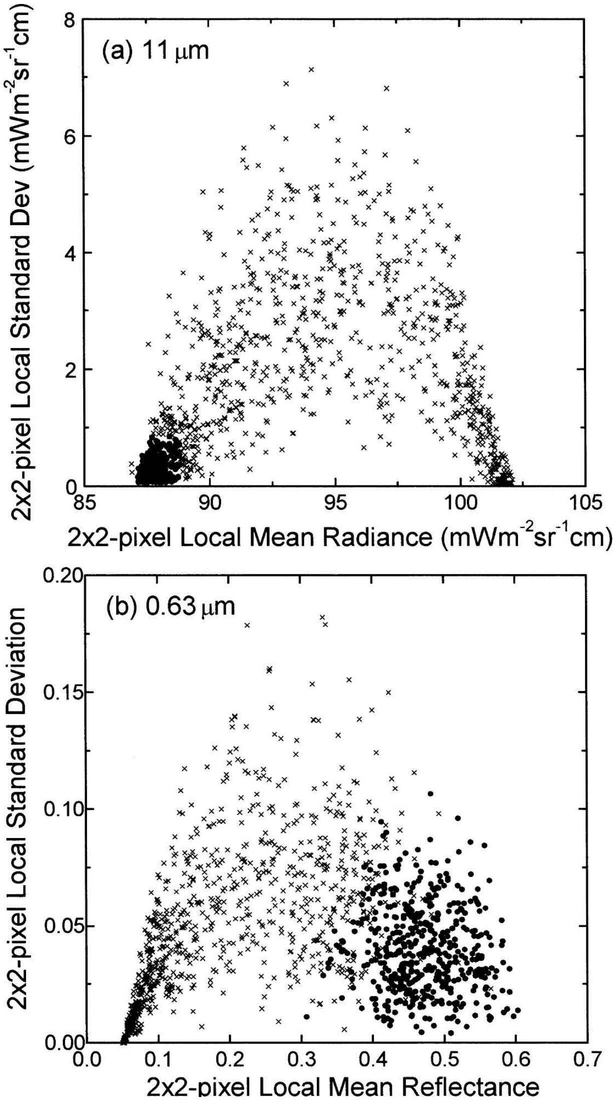

FIG. 1. Local means and local standard deviations for 2 × 2 arrays of the 4-km AVHRR GAC pixels (a) 11-μm radiances and (b) 0.63-μm reflectances. The observations are for a 250-km area near the coast of Chile. Solid circles indicate pixels overcast by clouds that are part of a single-layer cloud system. Each point represents an 8-km area.

ground. More details of the method and criteria for the selection of overcast pixels are discussed in Coakley and Baldwin (1984).

In addition to the spatial coherence method, results were obtained by applying radiance thresholds to both the 0.63-μm reflectance ($R_s + \Delta R$) and the 11-μm brightness temperature ($T_s - \Delta T$). Following ISCCP procedures for open oceans (Rossow et al. 1991), the thresholds were set at $\Delta R = 0.03$ and $\Delta T = 3$ K. For reflectances, the values obtained from the AVHRR level 1B data were normalized by the cosine of the solar zenith angle. The 0.63-μm cloud-free reflectance R_s, typically ~0.06, and the 11-μm cloud-free brightness temperature, T_s, were obtained based on the spatial coherence analysis.

Figure 1b shows the local means and local standard deviations of the AVHRR 0.63-μm reflectance associated with the 2 × 2 pixel arrays shown in Fig. 1a. The 0.63-μm cloud-free reflectances are around 0.05–0.06. The 0.63-μm overcast radiances (solid circles), on the other hand, show considerable variability caused by pixel-to-pixel variability in cloud liquid water. The threshold cloudy pixels were selected when both the AVHRR 0.63-μm reflectance was larger than $R_s + \Delta R$ and the AVHRR 11-μm brightness temperature was colder than $T_s - \Delta T$. Clearly, the threshold cloudy pixels included both overcast and partly cloudy pixels.

b. Cloud property retrievals

Cloud visible optical depth, τ, layer temperature, T_c, and droplet effective radius, r_e, were retrieved for each pixel identified as overcast by the spatial coherence method and each pixel identified as cloudy by the threshold method. Retrievals were performed only for pixels observed at a near-nadir satellite viewing angle < 30° to reduce view-angle-dependent biases (Loeb and Coakley 1998) that arise through the application of plane-parallel radiative transfer theory, as is done here. Following Tselioudis et al. (1992), only low-level marine clouds with a cloud-top temperature greater than the 680-hPa atmospheric temperature were analyzed.

The retrievals of τ, T_c, and r_e involve the searches of lookup tables generated by plane-parallel radiative transfer modeling. The retrieval algorithm follows the versions used by Chang et al. (2000) and Coakley et al. (2000) and is similar to the schemes used by Platnick and Twomey (1994) and Han et al. (1994). In the radiative transfer calculations, the atmosphere was divided into 13 vertical layers. A 32-stream (16 up and 16 down) adding–doubling method (Goody and Yung 1989) was used for generations of the lookup tables for the 0.63-, 3.7-, and 11-μm channels. The calculations accounted for the effects of molecular scattering and absorption within the AVHRR channels (Kratz 1995). Mie scattering phase functions for water droplets were approximated using 32 moments of the Legendre polynomial expansions. A delta-M method was used to account for the forward peak of the scattering phase functions (Wiscombe 1977). A gamma size distribution with effective variance of 0.13 was adopted for the droplet size distribution (Hansen and Travis 1974).

Four lookup tables were generated for the 0.63- and 3.7-μm reflectances and the 3.7- and 11-μm emittances. Both 0.63- and 3.7-μm reflectances were generated for

16 solar zenith and 16 satellite zenith angles (at Gauss quadrature points), 19 relative azimuth angles (0°, 10°, . . . , 180°), 16 values of the cloud optical depth (τ = 0.2, 0.5, . . . , 128), 16 values of the effective droplet radius (r_e = 3 μm, 4 μm, . . . , 32 μm), and 5 values of the cloud-top altitude (z_{top} = 0 km, 1 km, . . . , 6 km). The 3.7- and 11-μm emission lookup tables were generated for 16 satellite zenith angles, 16 values of the visible optical depth, 16 values of the droplet effective radius, and 5 values of the cloud-top altitude. Emission was calculated using the model-layer emissivity and the Planck function at the layer mean temperature. Sea surface and atmospheric temperatures and humidity profiles were obtained from the ISCCP version of the National Oceanic and Atmospheric Administration (NOAA) Television Infrared Observation Satellite (TIROS) Operational Vertical Sounder (TOVS) data product at a 2.5° grid scale (Rossow et al. 1991). Ozone column abundance data were also obtained from the TOVS, but the ozone absorption was assumed to occur in the uppermost layer of the model. The solar irradiance data were taken from Thekaekara (1974) and the AVHRR spectral response functions were from Kidwell (1991). Lambertain ocean surface reflectance of 0.06 at 0.63 μm and 0.03 at 3.7 μm were assumed. Aerosol effects were assumed to be included in the surface background reflectance. Postlaunch calibrations for the 0.63-μm reflectances were taken from Rao and Chen (1995). The absolute uncertainty in 0.63-μm reflectance is about ±0.01–0.02. The uncertainty in the 3.7- and 11-μm brightness temperatures is about ±1–2 K for temperatures larger than 270 K. Here the level 1B calibration coefficients were applied to the 3.7- and 11-μm radiances (Kidwell 1991).

The retrieval algorithm employed an iterative procedure as follows:

1) Start with initial values of r_e = 10 μm and z_{top} = 1 km.
2) Derive the cloud 0.63-μm cloud optical depth based on the comparison of the 0.63-μm reflectance with the values in the lookup table.
3) Derive T_c and the associated z_{top} by comparing the 11-μm radiance with values in the lookup table associated with the derived optical depth, τ and the droplet effective radius, r_e.
4) Derive the emission at 3.7 μm based on the lookup table for 3.7-μm emission obtained with τ, r_e, T_c, and z_{top}.
5) Derive the 3.7-μm reflectance by subtracting the 3.7-μm emission from the 3.7-μm radiance.
6) Derive the droplet effective radius, r_e, by comparing the 3.7-μm reflectance with values in the lookup table for the given τ and z_{top}.

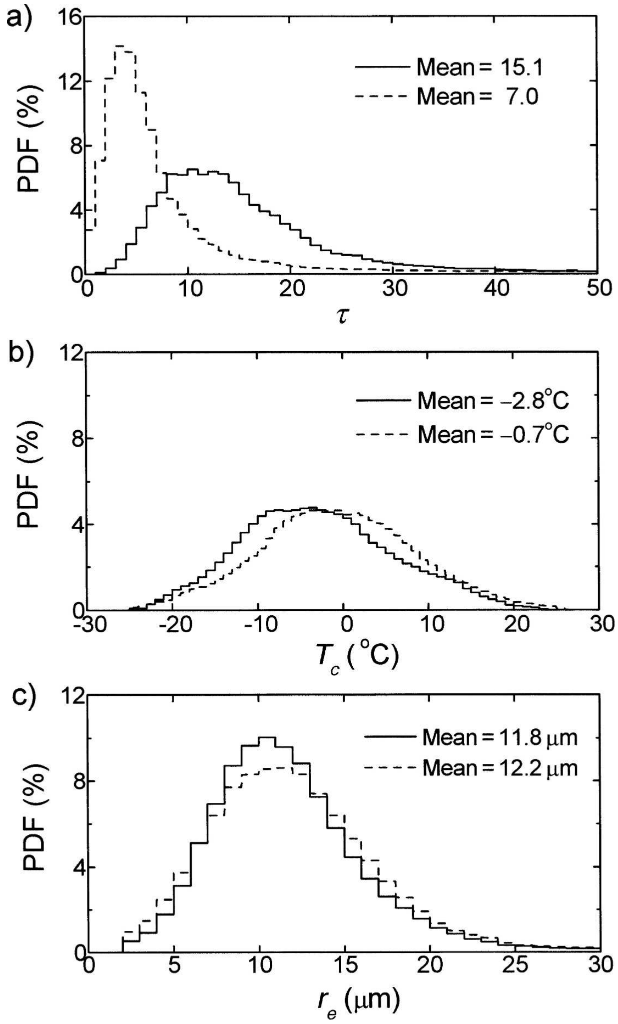

FIG. 2. Probability density functions of (a) τ, (b) T_c, and (c) r_e for the overcast pixels (solid) and partly cloudy pixels (dashed) obtained over the northern Pacific Ocean between 25° and 55°N. Mean values are indicated in each panel.

7) Repeat steps (2)–(6) until the changes in *4*, r_e, T_c, and z_{top} reach convergence.

Convergence was often achieved within two–three iterations.

3. Results and discussions

a. *Comparisons between overcast and threshold cloud properties*

Figure 2 shows the probability distribution functions (PDFs) of the AVHRR-retrieved cloud optical depths, τ (2a), cloud layer temperatures, T_c (2b), and droplet effective radii, r_e (2c), obtained for the overcast pixels (solid lines) and threshold cloudy pixels (dashed lines)

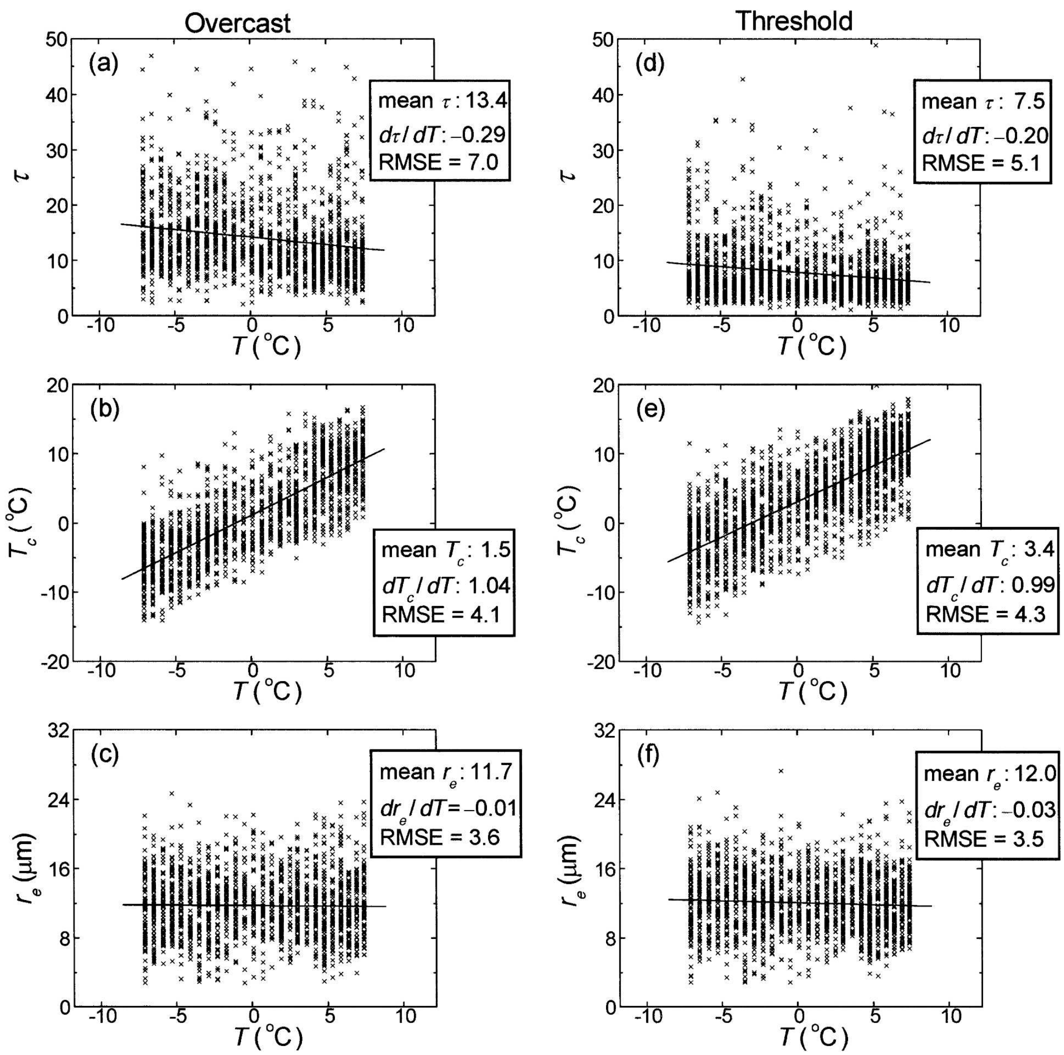

FIG. 3. Cloud properties (a), (d) τ, (b), (e) T_c, and (c), (f) r_e for the (a)–(c) overcast and (d)–(f) threshold clouds vs the 740-hPa air temperature for $-7.5°C < T < +7.5°C$ obtained over the northern Pacific Ocean between 25° and 55°N. Each data value represents a 2.5° latitude × longitude daily mean. The overall mean cloud properties, the slopes of linear regression fits, and the RMSE of the fits are indicated in each panel.

based on the spatial coherence analysis of single-layer clouds obtained between 25° and 55°N. In the retrievals of τ, T_c, and r_e, all threshold cloudy pixels were assumed to be completely overcast. Mean values of τ, T_c, and r_e for the spatial coherence overcast pixels and the threshold cloudy pixels are given in the figure. The threshold cloud retrievals produced systematically smaller optical depths than the overcast cloud optical depths (Fig. 2a). Likewise, the threshold cloud retrievals produced systematically warmer cloud temperatures than the overcast cloud temperatures (Fig. 2b). There were small differences in droplet effective radii between the overcast and threshold cloud retrievals (Fig. 2c), but the mean value and the spread of the radius distribution for the threshold pixels were slightly larger. The reason for the small differences in droplet effective radii may be due to error cancellations by both reflectance errors and emission errors, which offset each other at the 3.7-μm channel. There were losses in pixel-scale 3.7-μm reflectance due to partially cloudy cover and gains in pixel-scale 3.7-μm emission due to partially cloud-free area with warm sea surface temperature.

The pixel-scale τ, T_c, and r_e were averaged to calculate mean values for each 2.5° latitude × 2.5° longitude region. Two different sets of mean values for τ, T_c, and r_e were calculated: 1) "overcast"—from the spatial coherence overcast pixels, and 2) "threshold"—from the threshold cloudy pixels that included all partly cloudy and overcast pixels. Figure 3 shows an example in comparing the 2.5°-mean overcast τ (3a), T_c (3b), and r_e (3c)

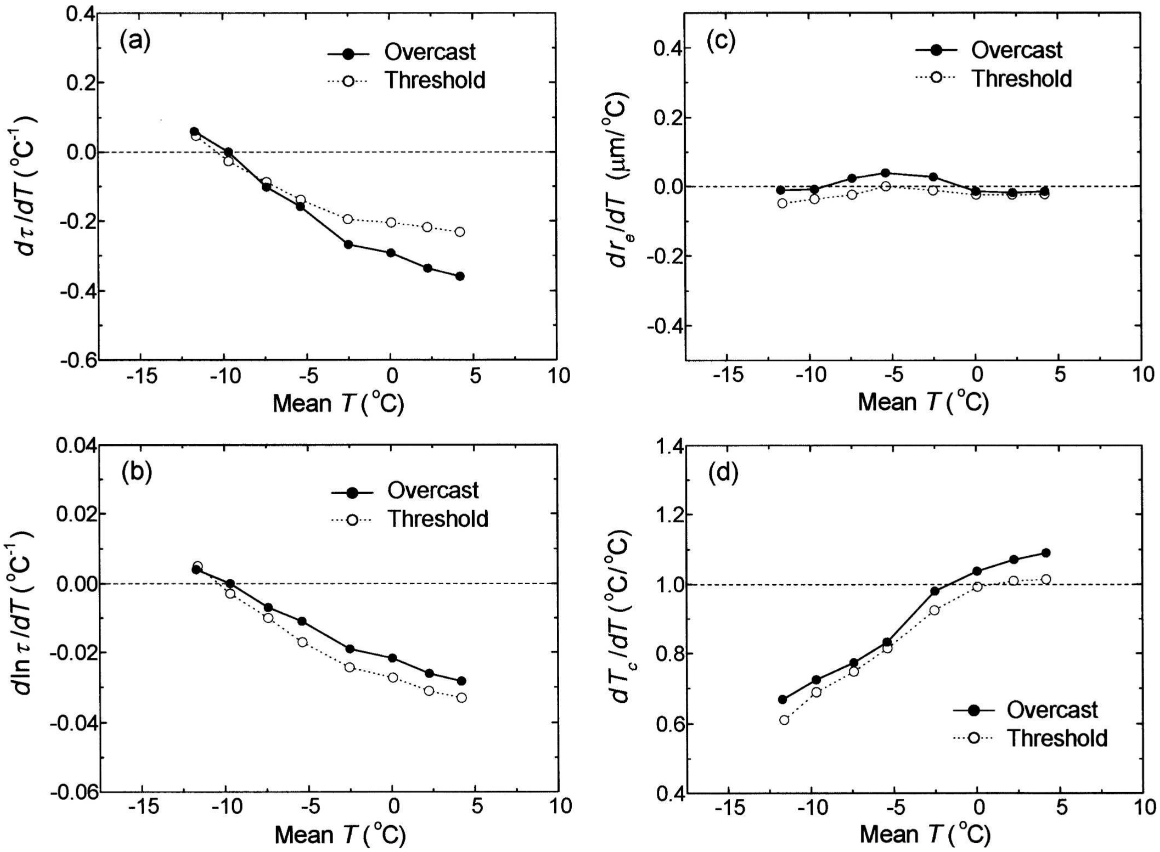

FIG. 4. (a) $d\tau/dT$, (b) $d\ \ln\tau/dT$, (c) dr_e/dT, and (d) dT_c/dT as functions of mean T obtained for the northern Pacific Ocean between 25° and 55°N. Solid circles are for the overcast and open circles are for threshold clouds.

versus the 2.5°-mean threshold τ (3d), T_c (3e), and r_e (3f) obtained between 25° and 55°N, which is plotted against their corresponding 2.5°-mean 740-hPa temperature, T, for the intervals of $-7.5°C < T < +7.5°C$. Clearly, the overcast τ values in Fig. 3a were systematically larger by nearly a factor of 2 than their threshold counterparts in Fig. 3d; the overcast T_c values in Fig. 3b were systematically smaller by ~2°C than their threshold counterparts in Fig. 3e; and the overcast r_e values in Fig. 3c were slightly smaller than their threshold counterparts in Fig. 3f. Note that the percentage of the overcast pixels was about 35% of the threshold cloudy pixels.

Also plotted in the figure are linear regression lines fitted to the data. Their slopes and root-mean-square errors (RMSEs) for the linear fit are given in each of the panels in Fig. 3. Despite the differences in magnitude between the overcast and threshold cloud retrievals, their linear regressions show similar trends, that is, both overcast and threshold cloud optical depths decreased (Figs. 3a,d) and both overcast and threshold cloud layer temperatures increased (Figs. 3b,e) as T increased. It is also similar between Fig. 3c and Fig. 3f: neither overcast nor threshold r_e values show a significant variation with T.

Figures 4a–d compare the overcast (solid points) and threshold (open points) values of $d\tau/dT$, $d\ \ln\tau/dT$, dT_c/dT, and dr_e/dT, respectively, derived for various 15°C intervals for the 25°–55°N region. The 15°C intervals were shifted every 2.5°C so that they overlapped. In comparing the signs of $d\tau/dT$ (Fig. 4a), dT_c/dT (Fig. 4d), and dr_e/dT (Fig. 4c), they are generally the same between the overcast and threshold values, but their magnitudes are different, especially in the case of $d\tau/dT$ (Fig. 4a) for warm temperatures. In Fig. 4b, the values for $d\ \ln\tau/dT$ (i.e., $\tau^{-1}d\tau/dT$) that were derived the same way as in Tselioudis et al. (1992) are plotted for comparisons. The magnitudes for $d\ \ln\tau/dT$ are much smaller (e.g., $\sim -0.02 - -0.04$) than the magnitudes for $d\tau/dT$ (e.g., ~ -0.3), but differences are larger between the overcast and threshold values for $d\tau/dT$.

For $d\ \ln\tau/dT$ (Fig. 4b), the threshold values (open points) are slightly more negative than the overcast values (solid points). The threshold values, like those obtained by Tselioudis et al. (1992) using ISCCP cloud products, are considered to some extent to be caused by

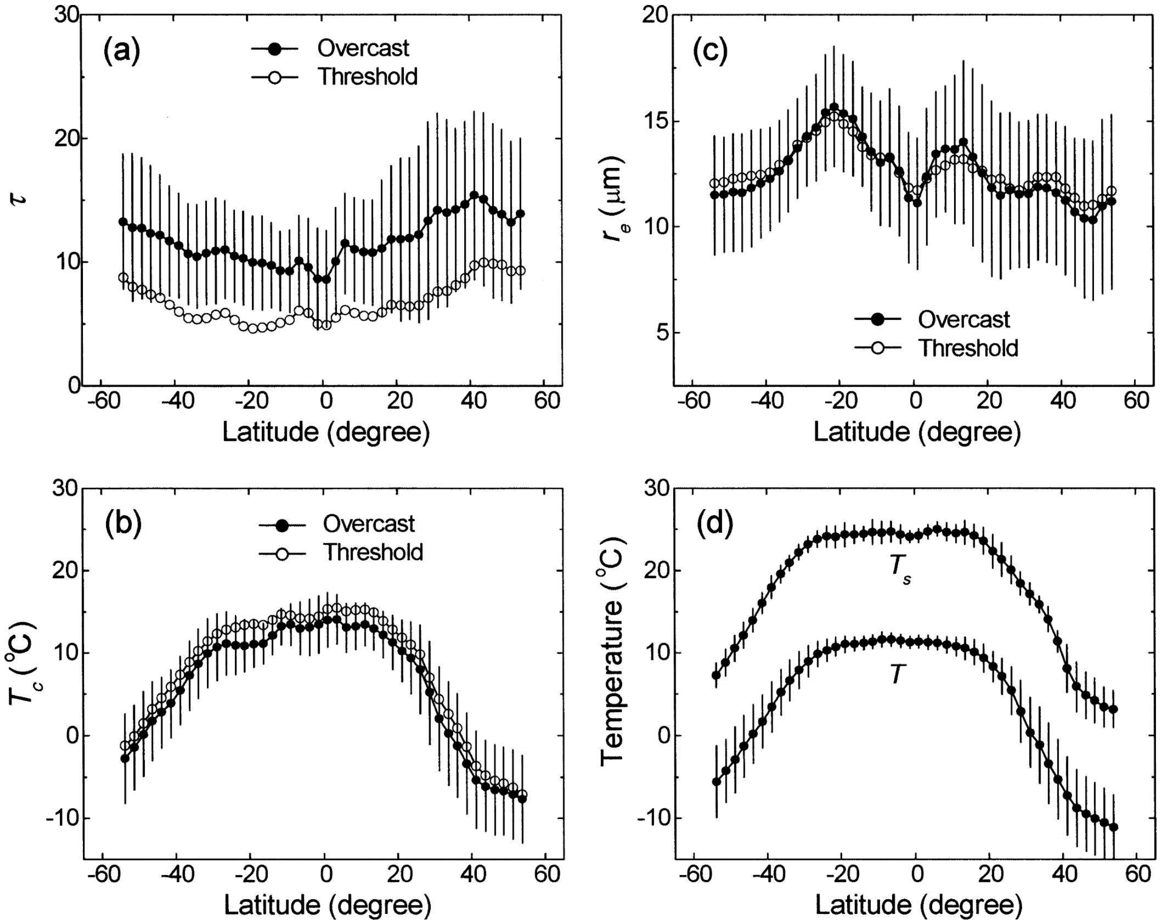

FIG. 5. Latitudinal mean overcast (solid circles) and threshold (open circles) cloud properties, (a) τ, (b) T_c, and (c) r_e; (d) latitudinal mean temperatures at sea surface, T_s, and 740 hPa, T. Error bars represent the standard deviations of the means, but they are not shown for the threshold clouds.

changes in cloud cover fraction for partly cloudy pixels. However, comparisons in Fig. 4b show that the logarithmic derivatives, $d\ln\tau/dT$, produced similar behaviors between the overcast and threshold values. Both of them changed progressively from positive values at cold temperatures ($T < -10°C$) to mostly negative values at warmer temperatures. The results obtained here for the northern Pacific Ocean agree with the results suggested by Tselioudis et al. (1992). The finding suggests there are strong correlations in the cloud properties between overcast and partly cloudy pixels despite the differences in their pixel-scale cloud cover fractions. Therefore, the negative relationships were little affected when partly cloudy pixels were assumed fully overcast.

For dT_c/dT (Fig. 4d), the threshold values (open points) are also slightly smaller than the overcast values. The values of dT_c/dT are generally smaller than 1.0 for cold temperatures and then increase progressively to values larger than 1.0 for warm temperatures ($T >$ 0°C). The values of $dT_c/dT < 1.0$ imply that cloud-top height, z_{top}, increases as the atmospheric temperature increases; whereas the values of $dT_c/dT > 1.0$ imply that cloud-top height decreases as the atmospheric temperature increases. For dr_e/dT (Fig. 4c), there appears to be no significant variation of r_e with T. Based on the statistics of the fits from which the derivatives were obtained, the uncertainty is about 0.03–0.05 for $d\tau/dT$, 0.003–0.005 for $d\ln\tau/dT$, 0.02–0.04 for dT_c/dT, and 0.01–0.02 for dr_e/dT.

Figures 5a–c show the overcast versus the threshold-derived 2.5° latitudinal means from 55°S to 55°N for cloud optical depths, τ, cloud layer temperatures, T_c, and droplet effective radii, r_e, respectively. The standard deviations associated with each of the 2.5° latitude means are also plotted. While they are only plotted for the overcast values to avoid confusion, the standard deviations for the threshold values are similar in magnitude to those plotted for the overcast values. Overall, the latitudinal distributions show that threshold cloud optical depths were 30%–50% smaller than overcast cloud optical depths, and threshold cloud layer temperatures were 1°−4°C higher than overcast cloud layer temperatures. Differences in droplet effective radii were relatively small (<1 μm) between the overcast and threshold values.

We find that the threshold cloud optical depths as shown in Fig. 5a (mean values of ~7.4 for the northern Pacific and ~6.0 for the southern Pacific) are comparable in magnitude to the ISCCP cloud optical depths as reported by Tselioudis et al. (1992), but as expected these values were significantly smaller than those for the overcast pixels (mean values of ~12.6 for the northern Pacific and ~10.8 for the southern Pacific). Values of the droplet effective radii shown in Fig. 5c are also similar to the values reported by Han et al. (1994), where droplet effective radii were on average ~1.3 μm smaller in the northern Pacific (mean values of ~11.8/11.9 for overcast/threshold) than in the southern Pacific (mean values of ~13.1/13.1 for overcast/threshold). Smaller droplet effective radii in the northern Pacific can be attributed to the effect of higher aerosol loadings in the Northern Hemisphere, as suggested by Han et al. (1994).

Figure 5d shows the latitudinal variations of 740-hPa atmospheric temperature, T, and sea surface temperature, T_s. In comparisons between Figs. 5b and 5d, patterns of the latitudinal variations of T_c follow the patterns of the latitudinal variations of T and T_s. The mean low-level cloud layer temperatures were about 14°C colder than the mean sea surface temperatures, which indicated about 2 km in mean altitudes for these low-level clouds. It is noted that the sea surface temperatures had very small variations (standard deviations less than 2°C within a latitudinal band). Therefore, values of τ, T_c, and r_e are not correlated to T_s in this study because the small variability in T_s prevents reliable estimates of their relationships to T_s. There are also smaller variations in the atmospheric temperatures in tropical regions. As such, the relationships between any of the cloud properties and temperature obtained near the tropical regions have less significance.

b. Relationships between cloud optical depth and temperature

Cloud optical depth, τ, is governed by cloud LWC, geometrical thickness, D, and droplet effective radius, r_e, and is directly correlated with LWC and D while inversely correlated with r_e. By approximations,

$$\tau = \frac{3}{2}\frac{\mathrm{LWC} \times D}{r_e}. \tag{1}$$

Taking the logarithmic derivatives of Eq. (1) with cloud temperature, T_c, gives that

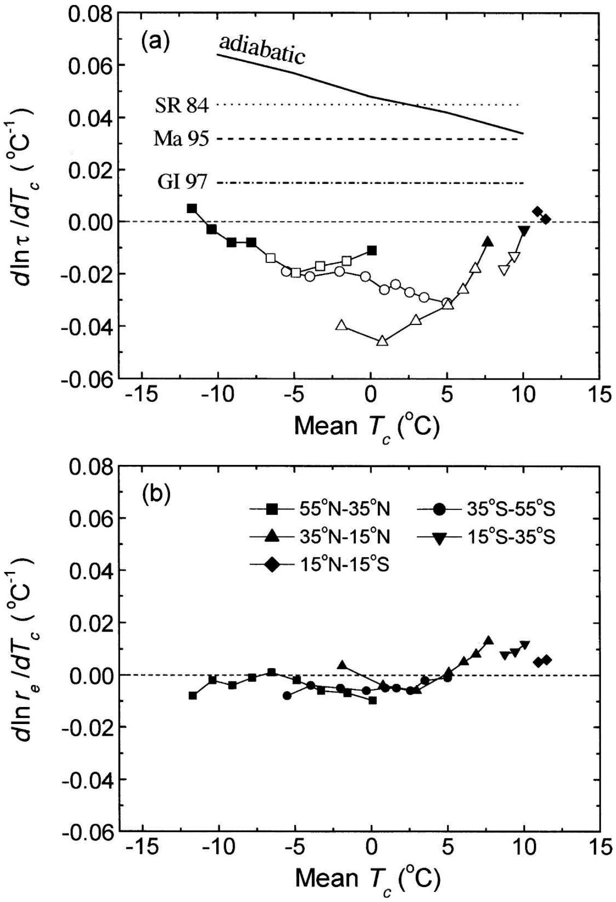

FIG. 6. (a) $d\ln\tau/dT_c$ and mean T_c for overcast clouds obtained over the northern midlatitudes (■, 55°–35°N), northern subtropics (▲, 35°–15°N), Tropics (◆, 15°N–15°S), southern subtropics (▼, 35°–15°S), and southern midlatitudes (●, 55°–35°S). Open symbols indicate correlation coefficients above the 95% significant level. Also, the empirical values obtained from Somerville and Remer [1984 (SR84), dotted], Mazin [1995 (Ma95), dashed], and Gultepe and Isaac [1997 (GI97), dashed–dotted] are plotted; (b) $d\ln r_e/dT_c$ and mean T_c for overcast clouds obtained for the five regions.

$$\frac{d\ln\tau}{dT_c} = \frac{d\ln(\mathrm{LWC})}{dT_c} + \frac{d\ln D}{dT_c} - \frac{d\ln r_e}{dT_c}. \tag{2}$$

There were few complete observational studies for determining the temperature-dependent relationships for cloud LWC, geometrical thickness, and droplet effective radius. Thus, $d\ln\tau/dT_c$ and $d\ln(\mathrm{LWC})/dT_c$ are often related by $d\ln D/dT_c = 0$ and $d\ln r_e/dT_c = 0$.

Here we examine the relationships between the cloud optical depth, τ, and cloud temperature, T_c, for only the overcast clouds due to potential biases in threshold cloud retrievals. Figure 6a shows the values of the overcast $d\ln\tau/dT_c$ derived for the 15°C intervals in T_c from five different regions: northern midlatitudes (■, 55°–35°N), northern subtropics (▲, 35°–15°N), Tropics (◆, 15°N–15°S), southern subtropics (▼, 35°–15°S), and southern midlatitudes (●, 55°–35°S). In the figure, open symbols indicate correlation coefficients above the 95% significant level and filled symbols indicate correlation coefficients below the 95% significance level. These overcast $d\ln\tau/dT_c$ show generally negative values and the magnitudes of $d\ln\tau/dT_c$ derived here for the northern midlatitudes (■, mean T_c between $-12°$ and 0°C) and for the northern subtropical (▲, mean T_c between $-2°$ and 7°C) are not much different from those reported by Tselioudis et al. (1992). For the Tropics (◆, mean T_c ~11°C), small positive values are shown in Fig. 6a, but Tselioudis et al. show large negative values of $d\ln\tau/dT_c \sim -0.04$. However, in the Tropics correlation coefficients for $d\ln\tau/dT_c$ were less significant in both studies. We also find generally negative values of $d\ln\tau/dT_c$ for the southern midlatitudes (●, mean T_c between $-6°$ and 5°C) and southern subtropics (▼, mean T_c between 8° and 10°C), except the magnitude is smaller around -0.02.

Figure 6a also shows the ranges of the adiabatic values (solid line) from Betts and Harshvandhan (1987) and three empirical values deduced from Somerville and Remer (1984), Mazin (1995), and Gultepe and Isaac (1997) based on aircraft measurements, which were approximated by $d\ln(\mathrm{LWC})/dT_c$ using Eq. (2) while assuming both $d\ln D/dT_c = 0$ and $d\ln r_e/dT_c = 0$. The value inferred from Somerville and Remer (1984), ~0.045 (dotted line), was derived based on Feigelson's (1978) study, which contained ~20 000 data measured during 1958–63 in the former Soviet Union; the value inferred from Mazin (1995), ~0.032 (dashed line), was also measured in the former Soviet Union and contained ~145 000 data measured during 1978–84; whereas the value inferred from Gultepe and Isaac (1997), ~0.015 (dashed–dotted line), was derived based on a more recent study and contained ~211 000 data measured during 1984–93 in the northeastern North America in Canada and in the United States. These studies used different LWC probes, and all measurements were made over land, except that in the Gultepe and Isaac study some maritime stratus clouds were also measured during the North Atlantic Regional Experiment (1993) and the Canadian Atlantic Storm Program (1992). Various factors, like different LWC probes and measuring strategies, may affect the uncertainty in aircraft LWC measurements (Gultepe and Isaac 1997). Here we use the value of $d\ln(\mathrm{LWC})/dT_c$ from Gultepe and Isaac as a constraint of minimum subadiabatic value and use the adiabatic values from Betts and Harshvandhan as a constraint of maximum.

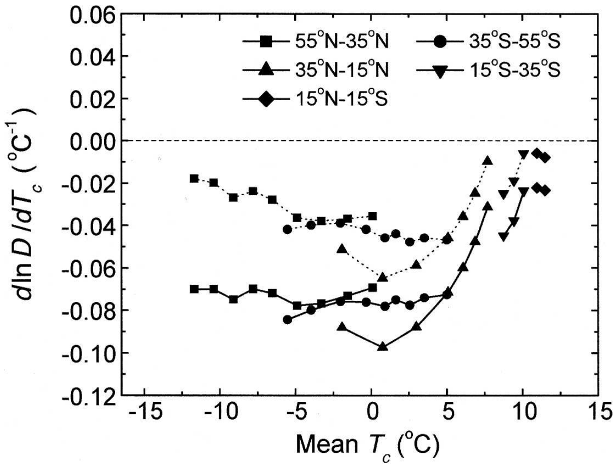

FIG. 7. Same as in Fig. 6b, but for two groups of $d\ln D/dT_c$ that were obtained based on the adiabatic assumption (symbols with solid lines) and assumption of a subadiabatic value (symbols with dotted lines).

Since the values of $d\ln(\mathrm{LWC})/dT_c$ inferred from the adiabatic process and from aircraft LWC measurements are all positive, the generally negative values of $d\ln\tau/dT_c$ inferred from the satellite observations ought to be due to variations in $d\ln D/dT_c$ and/or $d\ln r_e/dT_c$. Figure 6b shows the values of $d\ln r_e/dT_c$ derived from the same five regions as in Fig. 6a for the overcast clouds. There are no statistically significant correlations between r_e and T_c for these observations, and yet $d\ln r_e/dT_c$ needs to be positive in order to have a negative effect on $d\ln\tau/dT_c$. As a result, the negative value of $d\ln\tau/dT_c$ ought to result from a negative value of $d\ln D/dT_c$, according to Eq. (2). Unfortunately, the satellite data cannot provide direct measurements for the changes in D.

To evaluate the ranges of variations in $d\ln D/dT_c$ that are needed to produce the magnitude of the negative values in $d\ln\tau/dT_c$, we calculated $d\ln D/dT_c$ using Eq. (3):

$$\frac{d\ln D}{dT_c} = \frac{d\ln\tau}{dT_c} + \frac{d\ln r_e}{dT_c} - \frac{d\ln(\mathrm{LWC})}{dT_c}. \tag{3}$$

The values for $d\ln\tau/dT_c$ and $d\ln r_e/dT_c$ are taken from Figs. 6a and 6b, whereas values for $d\ln(\mathrm{LWC})/dT_c$ are assumed and taken to be 1) the adiabatic value as a maximum and 2) the subadiabatic value from Gultepe and Issac as a minimum. These calculated $d\ln D/dT_c$ are shown in Fig. 7, in which calculations made with the adiabatic value are plotted in symbols with solid lines and calculations made with the subadiabatic value are plotted in symbols with dotted lines. As expected, ranges of these calculated $d\ln D/dT_c$ values in Fig. 7 indicate negative values.

The negative $d\ln D/dT_c$ implies that, for instance, cloud geometrical thickness in midlatitudes would have decreased by 0.07–0.08 km (symbols with solid lines) per kilometer cloud thickness if the LWC varied at the adiabatic rate of change, or by 0.03–0.04 km (symbols with dotted lines) per kilometer cloud thickness if the LWC varied at the subadiabatic rate of change inferred from the Gultepe and Isaac data. These estimated negative values of $d\ln D/dT_c$ are quite large in magnitude, suggesting that the negative cloud optical depth–temperature relationships were dominated by the negative cloud geometrical thickness–temperature relationships. A few earlier studies on the diurnal cycle of marine stratocumulus layer have found that the stratocumulus cloud layer rose as sea surface temperature increased (Bougeault 1985; Betts and Boers 1990; Hignett 1991). This is because the temperature increase can cause increase in boundary layer depth and the cloud layer became more decoupled from the lower boundary layer moist air (Wyant et al. 1997). These may lead to cloud-base rising and hence to decreased cloud geometrical thickness.

Figures 8a–c show the latitudinal variations of $d\ln\tau/dT_c$, $d\ln r_e/dT_c$, and $d\ln D/dT_c$, respectively, between 55° and 15°S and between 15° and 55°N. Here tropical regions are excluded because of small variations in temperatures. The values are given for each of the 2.5° latitude bands and are obtained for overcast pixels. Values of $d\ln D/dT_c$ are derived following the procedure as described in Fig. 7. In contrast, Figs. 9a–c show similar latitudinal variations of $d\ln\tau/dT$, $d\ln r_e/dT$, and $d\ln D/dT$, respectively, except that cloud properties of τ, r_e, and D are related to 740-hPa atmospheric temperature, T. Differences between Figs. 8 and 9 in the derived temperature dependences of τ, r_e, and D to T_c are generally small. They show significantly negative cloud optical depth–temperature relationships (Figs. 8a and 9a) and negative cloud geometrical thickness–temperature relationships (Figs. 8c and 9c) in the midlatitudes between 20° and 55° in both hemispheres. These negative relationships also tend to change to positive lower and higher latitudes, but the evidence here is weak to support such arguments.

We take one step further to examine the latitudinal variations of dT_c/dT for inferences of variations in cloud-top height. Figure 10a shows the latitudinal variations of dT_c/dT derived from 55°S to 55°N. Values of dT_c/dT are mostly less than 1.0, except larger than 1.0 in the subtropics between 35° and 18°S and between 22° and 32°N. The variations in dT_c/dT are better reflected in terms of the variations of cloud-top height, z_{top}, with temperature, which are plotted in Fig. 10b for values of dz_{top}/dT. These values of dz_{top}/dT were calculated based on dT_c/dT using Eq. (4) by employing a constant lapse rate of $\Gamma = -7.1$°C/km (Betts et al. 1992; Minnis et al. 1992), given by

$$\frac{dz_{top}}{dT} = \left(\frac{dT_c}{dT} - 1\right)\frac{1}{\Gamma}. \tag{4}$$

As shown in Fig. 10, z_{top} increases with T when $dT_c/dT <$ 1.0; it decreases with increasing T when $dT_c/dT >$ 1.0. The results suggest that cloud-top altitude generally increases with warming, except in the subtropical regions where z_{top} decreased. It appears that in the sub-

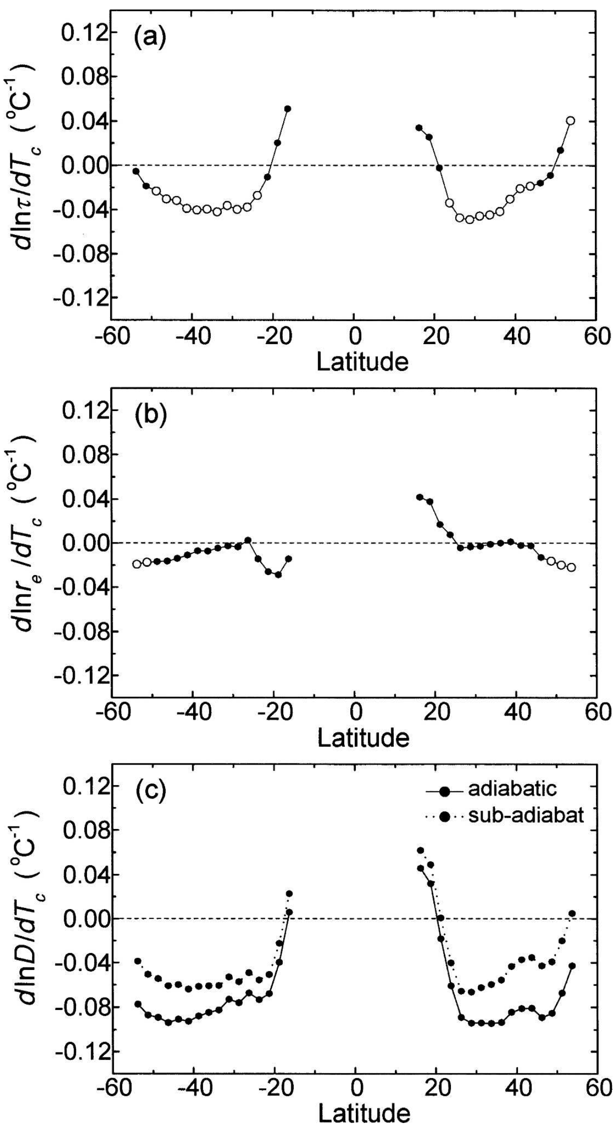

FIG. 8. Latitudinal variations of (a) $d\ln\tau/dT_c$, (b) $d\ln r_e/dT_c$, and (c) $d\ln D/dT_c$ for overcast clouds. The two different values of $d\ln D/dT_c$ were obtained with the adiabatic assumption (symbols with solid lines) and assumption of a subadiabatic value (symbols with dotted lines).

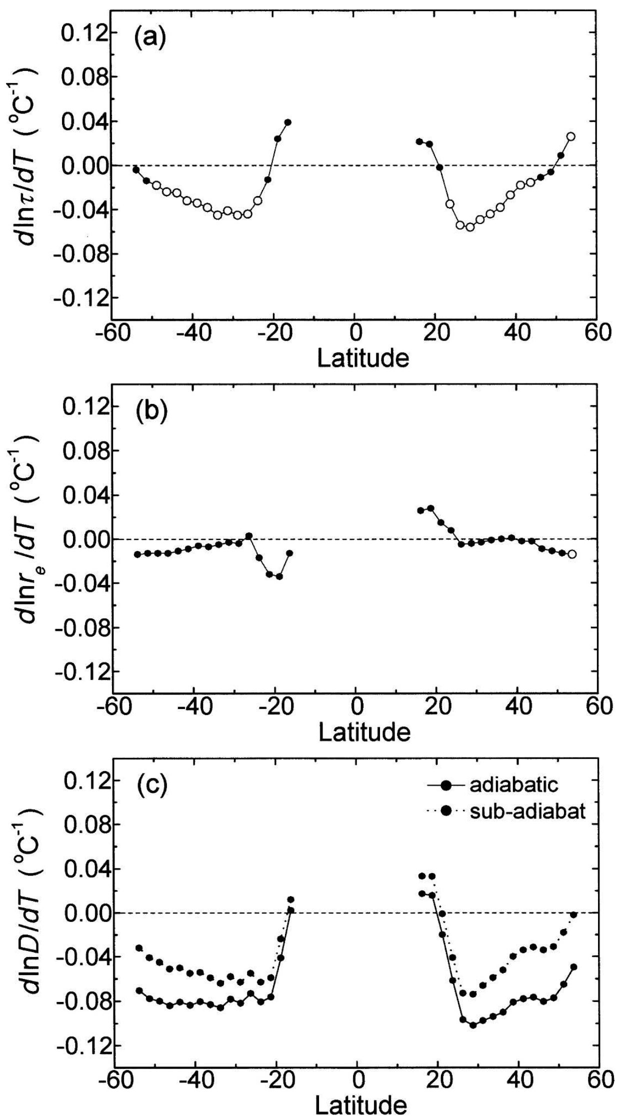

FIG. 9. Same as in Fig. 8, but the logarithmic derivatives are derived with respect to atmospheric temperature T.

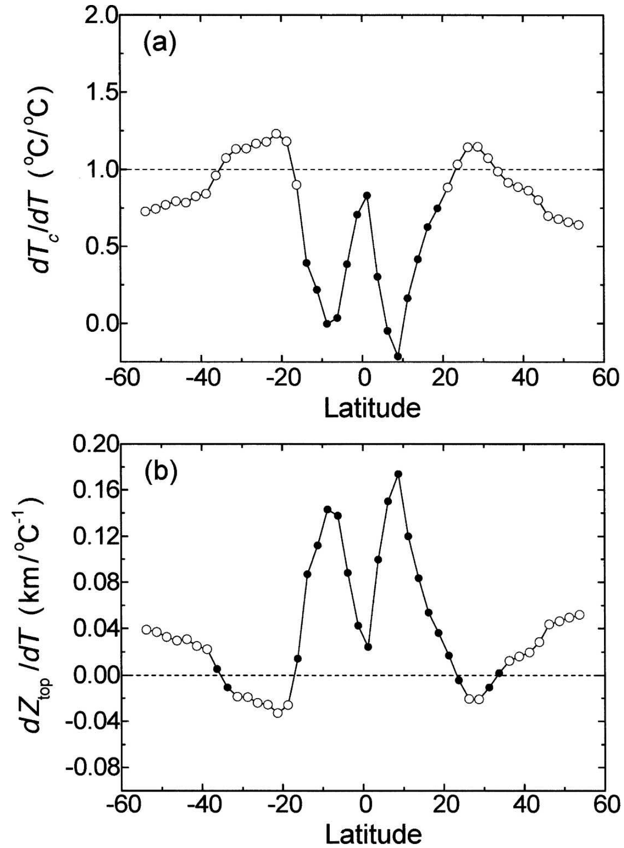

FIG. 10. Latitudinal variations of (a) dT_c/dT and (b) dz_{top}/dT obtained for the overcast clouds. Open symbols indicate correlation coefficients above the 95% significance level.

tropics the descending motions by the large-scale circulation may play a role in the variations of cloud altitude.

With findings of the cloud-top height increasing and cloud thickness decreasing, they imply that cloud-base height should have risen with warming. This inference suggests that the main reason why cloud optical depth decreases with warming is the ascending of the cloud base. Cloud-base ascending is due to the increase in the lifting condensation level, which may be caused by a reduction in the relative humidity below cloud layer as temperature increases (Del Genio and Wolf 2000). The decreases of z_{top} between 35° and 18°S and between 22° and 32°N as shown in Fig. 10b may also help explain the decreases in cloud thickness and optical depth in these latitudes. The large positive values of dz_{top}/dT as seen in the Tropics near 5°–10°S and 5°–10°N may imply increases in both cloud-top height and cloud thickness in these regions, but these implications require more rigorous studies.

4. Conclusions

This study applies the spatial coherence method to one month of AVHRR satellite data over the Pacific Ocean in order to differentiate overcast pixels from partly cloudy pixels and to reexamine the relationships between cloud optical depth and temperature for low-level marine stratus clouds. We find that, for the low-level marine stratus clouds studied here, the optical depths retrieved for the partly cloudy pixels, when assuming that they are overcast, were systematically smaller than those for the overcast pixels by about 30%–50%; likewise, the cloud layer temperatures for the partly cloudy pixels were systematically higher by about 1°–4°C and the droplet effective radii for the partly cloudy pixels were slightly larger. These differences were easily detected since partly cloudy pixels occur in a large percentage (>60%) of the satellite pixels (Chang and Coakley 1993).

Differentiating the overcast pixels from those partly cloudy pixels is necessary in reexamining the negative cloud optical depth and temperature relationships reported earlier by Tselioudis et al. (1992), in which they analyzed the ISCCP-retrieved properties for low-level clouds and reported that cloud optical depth often decreases with increasing temperature. This satellite result is contrary to the earlier idea that cloud liquid water content (LWC) would increase with temperature for constant cloud physical thickness to provide a negative cloud optical depth feedback as climate warms. Since ISCCP cloud properties are based on the threshold assumption that partly cloudy pixels were treated as being overcast, the assumption can lead to underestimates in the retrieved cloud optical depth and overestimates in the retrieved cloud temperature. If a region went from largely overcast to broken clouds as temperature increased, the partly cloudy pixels can be one reason why the threshold-retrieved cloud properties lead to the negative cloud optical depth and temperature relationships.

Interestingly, we find that the optical depths of overcast pixels indeed decreased with increased temperature, and yet the cloud optical depth–temperature relationships obtained for the overcast pixels show similar behaviors to the negative relationships obtained by including all partly cloudy pixels. Also, the results of the negative cloud optical depth–temperature relationships obtained here agree quantitatively with the ISCCP analysis over the midlatitudes and subtropics. In the Tropics, we find slightly positive relationships, unlike the large negative values revealed in ISCCP data. However, correlations are weak in the tropical regions due to small changes in temperatures. The agreement between the overcast and partly cloud pixels in their negative cloud optical depth–temperature relationships suggests that, for these low-level marine stratus clouds, cloud thinning is the main cause for the decreased cloud optical depth with warming. It also suggests that this cloud thinning effect applies to both the overcast and partly cloudy pixels. This is not to say that biases in the retrievals for partly cloudy pixels do not affect the negative cloud optical depth–temperature relationships, rather that cloud thinning should be the dominant reason for these negative relationships.

The effect due to changes in droplet effective radius is examined where ISCCP retrievals of cloud optical depth and temperature assumed constant droplet effective radius. While a significant increase in droplet effective radius may partially explain the decrease in cloud optical depth, we did not find that in this study. In fact, we found slightly negative droplet effective radius and temperature relationships, but the magnitude of this effect is relatively small.

The effect of cloud thinning is due primarily to increases in cloud-base height causing decreases in cloud geometrical thickness. Behaviors of cloud thickness decreasing with increased temperature were observed in the Oklahoma Southern Great Plains ground site of the Atmospheric Radiation Measurement Program (ARM) by Del Genio and Wolf (2000), where they found that the decreases were most strongly in the summer with warm temperatures. The main reason why cloud geometrical thickness decreases is suggested to be the ascent of cloud-base height due to an increase in the lifting condensation level. Both modeling and observational studies indicate that increases in boundary layer depth associated with warming tend to make the stratocumulus cloud layer more decoupled from the sea surface and can thus inhibit the transport of warm moisture-laden parcels from near the sea surface (Nicholls 1984; Austin et al. 1995; Martin et al. 1995; Wyant et al. 1997). Other complications like the entrainment and evaporation effects at both cloud top and cloud base may also reduce the cloud thickness and possibly LWC as well (Albrecht et al. 1995).

Despite the cloud thickness decreasing with increasing temperature, cloud-top heights often do not decrease. In midlatitudes, cloud-top heights generally increase with atmospheric warming. This implies that the cloud elevation generally increases with increasing temperature. There were cloud-top height decreases in the subtropics and presumably they were linked to the descending branch of the large-scale circulation. The increases in cloud-base height, on the other hand, could be more a result of local dynamic and thermodynamic processes and were not associated with the large-scale forcing.

For the effect of cloud LWC variations with temperature, we have compared adiabatic values of LWC with some empirical values inferred from large ensembles of aircraft LWC measurements that are documented in the literature. There were very few complete databases that can be used for the analysis of cloud LWC and temperature relationships, which would require large volumes of in situ measurements covering a large range of temperature variations. Among them, the studies of Somerville and Remer (1984), Mazin (1995), and Gultepe and Isaac (1997) are presented for inferring the empirical relationships between cloud LWC and cloud temperature, T_c, from aircraft measurements, Unfortunately, the studies of Somerville and Remer and Mazin were based on measurements obtained over the former Soviet Union and the study of Gultepe and Isaac was based on measurements obtained over the northeast North America. They all represent midlatitude continental clouds. Nonetheless, these aircraft data indicate that cloud LWC increases with increasing temperature but rarely approaches the adiabatic value. Recent cloud field experiments over the northeast and southeast Pacific Ocean have suggested that drizzle is a common occurrence in marine stratocumulus cloud systems (Bretherton et al. 2004; Stevens et al. 2005; Sharon et al. 2006). Since drizzle can last for hours or days in the life cycles of marine stratocumulus clouds, this may be one important cloud process that reduces cloud LWC and alters cloud radiative properties.

The variations of cloud LWC and cloud optical depth with temperature are more complicated in the Tropics. Our results best represent the midlatitude regions. There is a lack of detailed observations of LWC for the Tropics. For this reason, this study has eliminated most analysis for the Tropics. Because LWC is an important parameter that relates to cloud optical properties and the dynamic and thermodynamic structures of clouds, it is obvious that improving the LWC parameterization in GCMs requires more complete observations on the LWC and temperature relationships. This information on the global scale is critical for the evaluation of cloud optical depth and temperature relationships and for improving the performance of GCMs.

Acknowledgments. This work was supported in part by the National Science Foundation through the Center for Clouds, Chemistry and Climate at the Scripps Institution of Oceanography and in part through NASA Grant NNG04GM11G. The authors are grateful to the journal editor and two reviewers for their helpful comments.

REFERENCES

Albrecht, B. A., C. S. Bretherton, D. Johnson, W. H. Scubert, and A. S. Frisch, 1995: The Atlantic Stratocumulus Transition Experiment—ASTEX. *Bull. Amer. Meteor. Soc.,* **76,** 889–904.

Austin, P., Y. Wang, R. Pincus, and V. Kujala, 1995: Precipitation in stratocumulus clouds: Observational and modeling results. *J. Atmos. Sci.,* **52,** 2329–2352.

Betts, A. K., and Harshvardhan, 1987: Thermodynamic constraint on the cloud liquid water feedback in climate models. *J. Geophys. Res.,* **92,** 8483–8485.

——, and R. Boers, 1990: A cloudiness transition in a marine boundary layer. *J. Atmos. Sci.,* **47,** 1480–1497.

——, P. Minnis, W. Ridgway, and D. F. Young, 1992: Integration of satellite and surface data using a radiative–convective oceanic boundary-layer model. *J. Appl. Meteor.,* **31,** 340–350.

Bougeault, P., 1985: The diurnal cycle of the marine stratocumulus layer: A higher-order model study. *J. Atmos. Sci.,* **42,** 2826–2843.

Bretherton, C. S., and Coauthors, 2004: The EPIC 2001 stratocumulus study. *Bull. Amer. Meteor. Soc.,* **85,** 967–977.

Cess, R. D., and Coauthors, 1990: Intercomparison and interpretation of climate feedback processes in 19 atmospheric general circulation models. *J. Geophys. Res.,* **95,** 16 601–16 615.

——, and Coauthors, 1996: Cloud feedback in atmospheric general circulation models: An update. *J. Geophys. Res.,* **101,** 12 791–12 794.

Chang, F.-L., and J. A. Coakley Jr., 1993: Estimating errors in fractional cloud cover obtained with infrared threshold methods. *J. Geophys. Res.,* **98,** 8825–8839.

——, Z. Li, and S. A. Ackerman, 2000: Examining the relationship between cloud and radiation quantities derived from satellite observations and model calculations. *J. Climate,* **13,** 3842–3859.

Coakley, J. A., Jr., and F. P. Bretherton, 1982: Cloud cover from high-resolution scanner data: Detecting and allowing for partially filled fields of view. *J. Geophys. Res.,* **87,** 4917–4932.

——, and D. G. Baldwin, 1984: Towards the objective analysis of clouds from satellite imagery data. *J. Appl. Meteor.,* **23,** 1065–1099.

——, and Coauthors, 2000: The appearance and disappearance of ship tracks on large spatial scales. *J. Atmos. Sci.,* **57,** 2765–2778.

——, M. A. Friedman, and W. R. Tahnk, 2005: Retrieval of cloud properties for partly cloudy imager pixels. *J. Atmos. Oceanic Technol.,* **22,** 3–17.

Cubasch, U., and Coauthors, 2001: Projections of future climate change. *Climate Change 2001: The Scientific Basis,* J.-W. Kim and J. Stone, Eds., Cambridge University Press, 526–582.

Del Genio, A. D., and A. B. Wolf, 2000: The temperature dependence of the liquid water path of low clouds in the southern Great Plains. *J. Climate,* **13,** 3465–3486.

Feigelson, E. M., 1978: Preliminary radiation model of a cloudy atmosphere. Part I: Structure of clouds and solar radiation. *Beitr. Phys. Atmos.,* **51,** 203–229.

Goody, R. M., and Y. L. Yung, 1989: *Atmospheric Radiation: Theoretical Basis.* 2d ed. Oxford University Press, 519 pp.

Gultepe, I., and G. A. Isaac, 1997: Liquid water content and temperature relationship from aircraft observations and its applicability to GCMs. *J. Climate,* **10,** 446–452.

Han, Q., W. B. Rossow, and A. A. Lacis, 1994: Near-global survey of effective droplet radii in liquid water clouds using ISCCP data. *J. Climate,* **7,** 465–497.

Hansen, J. E., and L. D. Travis, 1974: Light scattering in planetary atmospheres. *Space Sci. Rev.,* **16,** 527–610.

Harshvardhan, B. A. Wielicki, and K. M. Ginger, 1994: The interpretation of remotely sensed cloud properties from a model parameterization perspective. *J. Climate,* **7,** 1987–1998.

Hignett, P., 1991: Observations of diurnal variation in a cloud-capped marine boundary layer. *J. Atmos. Sci.,* **48,** 1474–1482.

Houghton, J. T., L. G. Meira Filho, B. A. Callander, N. Harris, A. Kattenberg, and K. Maskell, Eds., 1996: *Climate Change 1995: The Science of Climate Change.* Cambridge University Press, 572 pp.

Kidwell, K. B., 1991: NOAA polar orbiter data users guide. Satellite Data Services Division, NOAA/National Climate Data Center, 250 pp.

Kratz, D. P., 1995: The correlated-distribution technique as applied to the AVHRR channels. *J. Quant. Spectrosc. Radiat. Transfer,* **53,** 501–517.

Loeb, N. G., and J. A. Coakley Jr., 1998: Inference of marine stratus cloud optical depths from satellite measurements: Does 1D theory apply? *J. Climate,* **11,** 215–233.

Martin, G. M., D. W. Johnson, D. P. Rogers, P. R. Jonas, P. Minnis, and D. A. Hegg, 1995: Observations of the interaction between cumulus clouds and warm stratocumulus clouds in the marine boundary layer during ASTEX. *J. Atmos. Sci.,* **52,** 2902–2922.

Mazin, I. P., 1995: Cloud water content in continental clouds of middle latitudes. *J. Atmos. Res.,* **35,** 283–297.

Minnis, P., P. W. Heck, D. F. Young, C. W. Fairall, and J. B. Snider, 1992: Stratocumulus cloud properties derived from simultaneous satellite and island-based instrumentation during FIRE. *J. Appl. Meteor.,* **31,** 317–339.

Nicholls, S., 1984: The dynamics of stratocumulus: Aircraft observations and comparisons with a mixed layer model. *Quart. J. Roy. Meteor. Soc.,* **110,** 783–870.

Platnick, S., and S. Twomey, 1994: Determining the susceptibility of cloud albedo to changes in droplet concentration with the Advanced Very High Resolution Radiometer. *J. Appl. Meteor.,* **33,** 334–347.

Rao, C. R. N., and J. Chen, 1995: Inter satellite calibration linkages for the visible and near-infrared channels of the Advanced Very High Resolution Radiometer on the NOAA-7, -9, and -11 spacecraft. *Int. J. Remote Sens.,* **16,** 1931–1942.

Rossow, W. B., L. C. Garder, P. J. Lu, and A. Walker, 1991: International Satellite Cloud Climatology Project (ISCCP) documentation of cloud data. WMO Tech. Doc. 266 (revised), 76 pp.

Senior, C. A., and J. F. B. Mitchell, 1993: Carbon dioxide and climate: The impact of cloud parameterization. *J. Climate,* **6,** 393–418.

Sharon, T. M., B. A. Albrecht, H. H. Jonsson, P. Minnis, M. M. Khaiyer, T. M. van Reken, J. Seinfeld, and R. Flagan, 2006: Aerosol and cloud microphysical characteristics of rifts and gradients in maritime stratocumulus clouds. *J. Atmos. Sci.,* **63,** 983–997.

Somerville, R. C. J., and L. A. Remer, 1984: Cloud optical thickness feedbacks in the CO_2 climate problem. *J. Geophys. Res.,* **89,** 9668–9673.

Stephens, G. L., 2005: Cloud feedbacks in the climate system: A critical review. *J. Climate,* **18,** 237–273.

Stevens, B., G. Vali, K. Comstock, R. Wood, M. C. Van Zanten, P. H. Austin, C. S. Bretherton, and D. H. Lenschow, 2005: Pockets of open cells and drizzle in marine stratocumulus. *Bull. Amer. Meteor. Soc.,* **86,** 51–57.

Thekaekara, M. P., 1974: Extraterrestrial solar spectrum, 3000-6100A° at 1-A° intervals. *Appl. Opt.,* **13,** 518–522.

Tselioudis, G., and W. B. Rossow, 1994: Global, multiyear variations of optical thickness with temperature in low and cirrus clouds. *Geophys. Res. Lett.,* **21,** 2211–2214.

——, ——, and D. Rind, 1992: Global patterns of cloud optical thickness variation with temperature. *J. Climate,* **5,** 1484–1495.

Wielicki, B. A., E. F. Harrison, R. D. Cess, M. D. King, and D. A. Randall, 1995: Mission to Planet Earth: Role of clouds and radiation in climate. *Bull. Amer. Meteor. Soc.,* **76,** 2125–2153.

——, B. R. Barkstrom, E. F. Harrison, R. B. Lee III, G. L. Smith, and J. E. Cooper, 1996: Cloud and the Earth's Radiant Energy System (CERES): An Earth Observing System experiment. *Bull. Amer. Meteor. Soc.,* **77,** 853–868.

Wiscombe, W. J., 1977: The Delta-*M* method: Rapid yet accurate radiative flux calculations for strongly asymmetric phase functions. *J. Atmos. Sci.,* **34,** 1408–1422.

Wyant, M. C., C. S. Bretherton, H. A. Rand, and D. E. Stevens, 1997: Numerical simulations and a conceptual model of the stratocumulus to trade cumulus transition. *J. Atmos. Sci.,* **54,** 168–192.

Yao, M.-S., and A. D. Del Genio, 1999: Effects of cloud parameterization on the simulation of climate changes in the GISS GCM. *J. Climate,* **12,** 761–779.